

Probing the peak of star formation with the stochastic background of binary black hole mergers

NICO BERS^{1,2} AND SYLVIA BISCOVEANU^{1,*}

¹*Center for Interdisciplinary Exploration and Research in Astrophysics (CIERA), Northwestern University, 1800 Sherman Ave, Evanston, IL 60201, USA*

²*Department of Physics and Astronomy, Northwestern University, 2145 Sheridan Road, Evanston, IL 60201, USA*

ABSTRACT

Although the LIGO-Virgo-KAGRA collaboration detects many individually resolvable gravitational-wave events from binary black hole mergers, those that are too weak to be identified individually contribute to a stochastic gravitational-wave background. Unlike the standard cross-correlation search for excess correlated power, a Bayesian search method that models the background as a superposition of an unknown number of mergers enables simultaneous inference of the properties of high-redshift binary black hole populations and accelerated detection of the background. In this work, we apply this templated background search method to one day of simulated data at current LIGO Hanford-Livingston detector network sensitivity to determine whether the weakest mergers contribute information to the detection of the background and to the constraint on the merger redshift distribution at high redshifts. We find that the dominant source of information for the detection of the stochastic background comes from mergers with signal-to-noise ratios just below the individual detection threshold. However, we demonstrate that the weakest mergers do contribute to the constraint on the shape of the redshift distribution not only beyond the peak of star formation, but also beyond the redshifts accessible with individually detectable sources.

Keywords: astrophysical black holes — gravitational wave astronomy — gravitational wave sources

1. INTRODUCTION

The growing catalog of gravitational-wave events from merging compact-object binaries detected by the LIGO-Virgo-KAGRA (LVK) collaboration includes nearly 300 binary black hole (BBH) mergers, with over 200 such events observed during the ongoing fourth observing run (O4) (Abbott et al. 2023a; LIGO Scientific Collaboration 2024). These observations have revealed that stellar-mass binary black holes have component masses spanning the range $\sim 2\text{--}100 M_{\odot}$ (Fishbach & Holz 2017; Talbot & Thrane 2018; Abbott et al. 2023b; Tiwari & Fairhurst 2021; Edelman et al. 2022; Rinaldi & Del Pozzo 2021), generally small spins (Biscoveanu et al. 2021; Callister et al. 2022; Tong et al. 2022; Mould et al. 2022; Galadage et al. 2021; Roulet et al. 2021), and a merger rate distribution that is consistent with tracing the cosmic star formation history (Abbott et al. 2023b; Fishbach et al. 2021; Edelman et al. 2023; Payne &

Thrane 2023; Ray et al. 2023; Callister & Farr 2024). Constraints on the population-level properties of these systems provide clues to their formation and evolution. However, the current LVK detectors can only individually resolve BBH mergers out to $z \lesssim 2$ (Abbott et al. 2018a), which limits our ability to probe the properties of black holes at earlier cosmic epochs and to learn about how these properties evolve over time.

In addition to these individually-detectable sources, the LVK detectors (Aasi et al. 2015; Acernese et al. 2015; Aso et al. 2013; Somiya 2012; Akutsu et al. 2021) are sensitive to a stochastic gravitational-wave background (SGWB) originating from the superposition of unresolvable compact-object mergers. The SGWB is typically characterized by the dimensionless gravitational-wave (GW) energy density spectrum

$$\Omega_{\text{GW}}(f) \equiv \frac{d\rho_{\text{GW}}}{\rho_c d \ln f}, \quad (1)$$

where ρ_{GW} is the GW energy density between f and $f + df$, and ρ_c is the critical energy density needed to close the universe. The current best upper limit on Ω_{GW} in the band of ground-based GW detectors is

Corresponding author: Sylvia Biscoveanu
sbisco@northwestern.edu

* NASA Einstein Fellow

$\Omega_{\text{GW}}(25 \text{ Hz}) \leq 3.4 \times 10^{-9}$ for a spectrum described by $\Omega_{\text{GW}}(f) = \Omega_{\text{ref}}(f/f_{\text{ref}})^{2/3}$ (Abbott et al. 2021a), where $\alpha = 2/3$ is the power-law index expected for a background of unresolved compact-object mergers in the frequency range up to $\mathcal{O}(100)$ Hz (Rosado 2011; Regimbau 2011; Zhu et al. 2011; Abbott et al. 2018b). The detection and characterization of this background would allow us to learn about the properties of high-redshift sources inaccessible individually with current detector sensitivities.

Standard searches for the SGWB assume the background is Gaussian, stationary, isotropic, and unpolarized, although the latter three assumptions have been relaxed in previous analyses of LVK data (e.g., Callister et al. 2017; Abbott et al. 2018c; Mukherjee & Silk 2020; Abbott et al. 2021b; Martinovic et al. 2021). The optimal search for a signal described by these statistical assumptions involves cross-correlating the data from detector pairs that are sufficiently geographically separated to mitigate common sources of noise (although correlated sources of noise persist at large spatial separations; Thrane et al. 2013, 2014; Coughlin et al. 2016; Meyers et al. 2020; Himemoto & Taruya 2019; Janssens et al. 2023; Himemoto et al. 2023), such that the signal manifests as excess coherent power (Christensen 1992; Allen & Romano 1999; Romano & Cornish 2017; Matas & Romano 2021). However, the astrophysical SGWB from sub-threshold BBH mergers is not expected to satisfy the central limit theorem required for the assumption of Gaussianity, as the duration of these signals in the sensitive band of the LVK detectors is $\mathcal{O}(10)$ s, while the average time between mergers is $\mathcal{O}(100)$ s, instead producing a “popcorn-like” Poisson background (Abbott et al. 2018b). Thus, the standard cross-correlation search is suboptimal for the BBH background, leading to reduced search sensitivity and longer time-to-detection.

Several alternative search methods relaxing the assumption of Gaussianity have been proposed. While the intermittent search method proposed in Drasco & Flanagan (2003); Lawrence et al. (2023) models the background as a series of Gaussian “bursts,” the Bayesian templated background search (TBS) described in Thrane (2013); Smith & Thrane (2018) models the background as a series of individual compact-object mergers represented by a deterministic signal model that depends on the properties of the merger. By splitting the interferometer strain data into short segments, both searches seek to measure the duty cycle, ξ , which represents the fraction of analyzed data segments that contain a merger or the probability that any given segment contains a merger. The intermittent search is found to outperform the standard cross-correlation search, reducing

the time-to-detection for a BBH background by a factor of ~ 50 (Lawrence et al. 2023). By additionally taking into account the deterministic nature of the signal rather than modeling it as a stochastic process, the TBS is found to reduce the time-to-detection by a factor of $\mathcal{O}(1000)$ (Smith & Thrane 2018). The TBS represents the statistically optimal search for the SGWB from BBH mergers, at increased computational cost compared to the intermittent search, as full Bayesian inference is performed on each analyzed segment of data to obtain posterior probability distributions on the binary parameters characterizing a potential BBH signal in that stretch of data.

This allows for the simultaneous characterization of the population properties of the BBH sources contributing to the background along with the measurement of the duty cycle, another advantage of modeling the BBH background deterministically. Previous works have demonstrated that constraints on BBH population properties, such as their mass, redshift, and time delay distributions, could be extracted from the point estimate for $\Omega_{\text{GW}}(f)$ obtained using variations of the cross-correlation search (Zhu et al. 2011; Mandic et al. 2012; Callister et al. 2016; Safarzadeh et al. 2020; Mukherjee & Silk 2021; Sah & Mukherjee 2024; De Lillo & Suresh 2024; Kou et al. 2024). However, this is necessarily a statistically sub-optimal analysis, as the constraints on these properties come from their imprint on the aggregate $\Omega_{\text{GW}}(f)$ spectrum produced by that BBH population (e.g., Zhu et al. 2013; Renzini & Golomb 2024) rather than from combining the measurements of the properties of each individual BBH event using hierarchical inference (e.g., Thrane & Talbot 2019). A hybrid approach has also been demonstrated that combines the constraints on the BBH population properties obtained from resolved signals with those obtained from the (non)detection of the SGWB using the cross-correlation search (Callister et al. 2020; Lalleman et al. 2024; Turbang et al. 2024; Cousins et al. 2025; Ferraiuolo et al. 2025), but this method requires the arbitrary separation of BBH mergers into foreground and background.

Instead, the TBS allows for simultaneous detection and hierarchical inference of BBH population properties without imposing arbitrary thresholds on detection significance of individual events (see also Gaebel et al. 2019; Farr et al. 2015; Messenger & Veitch 2013). This avoids the issue of accounting for selection effects in hierarchical analyses (Loredo 2004; Mandel et al. 2019; Vitale et al. 2022), which are often a significant source of systematic uncertainty (e.g., Talbot & Golomb 2023; Essick & Fishbach 2024). Smith et al. (2020) demonstrated that informative constraints can be obtained on

the BBH mass and spin distributions using one week of data, but did not attempt to fit the redshift distribution. The ability to constrain the shape of the merger redshift distribution beyond the detection redshifts of individual events would imply that the most distant mergers contribute information to the detection and characterization of the background. However, the recent result of [Renzini et al. \(2024\)](#) using a Fisher matrix approach to conclude that the TBS obtains 99% of its information from merger redshifts $z < 1$ casts into doubt the ability of this method to shed light on the properties of high-redshift sources.

In this work, we instead take a Bayesian approach to determine where the TBS gets its information, modifying the original likelihood used in [Smith & Thrane \(2018\)](#) to incorporate selection effects (above or below a given threshold) to systematically exclude certain sources from the analysis in an unbiased way in Section 2. We also extend the threshold-less hierarchical inference analysis of [Smith et al. \(2020\)](#) to the BBH merger redshift distribution in Section 4. While we find that the information driving the posterior on ξ is indeed dominated by the segments with the loudest individual events in qualitative agreement with [Renzini et al. \(2024\)](#), we are able to obtain a meaningful constraint on the shape of the BBH redshift distribution past the peak of star formation where no individual sources are detected. This implies that while the weakest events do not contribute much information to the detection of the SGWB using the TBS, they do contribute information to the characterization of the underlying BBH population producing the background. Further discussion of the results and caveats of our analysis are presented in Section 5.

2. THE BAYESIAN TEMPLATED BACKGROUND SEARCH

We use the Bayesian templated background search (TBS) to measure the duty cycle for a simulated population of BBH mergers. To produce our population, we simulate data from the LIGO Hanford and Livingston detectors with the noise power spectral densities anticipated for their fourth observing run in 4 s segments ([Abbott et al. 2022](#)). This duration makes it very unlikely that more than one coalescence will occur in a single segment ([Smith & Thrane 2018](#)), given that BBH mergers occur every ~ 200 s in the Universe ([Abbott et al. 2018b](#)). We simulate data in the frequency domain with a frequency range of [20, 1024] Hz: 20520 Gaussian noise segments and 1080 segments with BBH merger signals generated with the IMRPHENOMPv2 waveform approximant ([Hannam et al. 2014](#)) in Gaussian noise,

meaning the population has an astrophysical duty cycle $\xi = 1080/21600 = 0.05$. To curtail the large computational cost of performing full Bayesian source characterization on each segment of data, we choose a duty cycle of $\xi = 0.05$, which is likely significantly larger than the value expected astrophysically. However, we will later demonstrate that our ability to constrain the population properties of high-redshift BBH depends only on the number of signal segments and is hence independent of the duty cycle.

Given that BBHs come from stellar progenitors, we expect that their merger redshift distribution roughly tracks the cosmic star formation history. The luminosity distances of the signals are thus sampled from the Madau-Dickinson distribution, which is parameterized in redshift as ([Madau & Dickinson 2014](#))

$$\psi(z|\gamma, \kappa, z_p) = \frac{(1+z)^\gamma}{1 + \left(\frac{1+z}{1+z_p}\right)^\kappa} \quad (2)$$

$$p(z|\gamma, \kappa, z_p) \propto \frac{1}{(1+z)} \frac{dV_c}{dz} \psi(z|\gamma, \kappa, z_p) \quad (3)$$

where dV_c/dz is the differential comoving volume, and $z_p = 1.9$, $\kappa = 5.6$, $\gamma = 2.7$. The distribution is composed of a broken power law that peaks near the redshift of the highest star formation rate, z_p . The slope of the distribution at low redshifts is parameterized by γ and at high redshifts by κ . We sample from $d_L \in [1, 29 \times 10^3]$ Mpc, corresponding to a maximum redshift of $z \approx 3.28$. The chirp masses are sampled from a power law distribution, $p(\mathcal{M}) \propto \mathcal{M}^{-3.5}$, $\mathcal{M} \in [40, 200]M_\odot$, where the inclusion of only high masses ensures that a full signal will fit entirely within our segment duration. The spin prior distribution is isotropic and uniform in magnitude, and the mass ratio prior is uniform over $q \in [0.125, 1]$. The shapes of these distributions are chosen to be consistent with current population inference models of BBHs ([Abbott et al. 2023b](#)) and to produce a sufficiently high number of both unresolved and resolved mergers at a manageable computational cost given the size of our simulated dataset, essential for analyzing the information within our population that contributes to the detection of the SGWB with the TBS.

We perform parameter estimation on all simulated data segments using BILBY, a Python-based Bayesian inference library ([Ashton et al. 2019](#); [Romero-Shaw et al. 2020](#)) and the DYNesty sampler ([Speagle 2020](#)), analytically marginalizing over the distance and phase parameters ([Thrane & Talbot 2019](#)). The priors used for parameter estimation are the same as those described above to generate individual BBH signals, and we use standard priors for the remaining unspecified extrinsic binary parameters ([Romero-Shaw et al. 2020](#)).

Using the signal and noise evidences obtained during sampling for each segment, $\mathcal{Z}_S^i = \mathcal{L}(d_i|S)$ and $\mathcal{Z}_N^i = \mathcal{L}(d_i|N)$, we calculate the posterior on the duty cycle, ξ , the proxy for detecting the SGWB. From Bayes' theorem, the posterior is

$$p(\xi|\{d\}) = \frac{\mathcal{L}(\{d\}|\xi)\pi(\xi)}{\mathcal{Z}}, \quad (4)$$

where the evidence, \mathcal{Z} , is the marginalized likelihood, $\pi(\xi)$ is a uniform prior on the duty cycle for $\xi \in [0, 1]$, and the total likelihood of the duty cycle over all n analyzed segments is (Smith & Thrane 2018)

$$\mathcal{L}(\{d\}|\xi) = \prod_i^n (\xi \mathcal{Z}_S^i + (1 - \xi) \mathcal{Z}_N^i), \quad (5)$$

where the index i indicates the individual data segment. Fig. 1 shows the signal-to-noise ratio (SNR) distribution for our simulated dataset, including both signal and noise segments. When referring to a SNR, unless otherwise specified, we refer to the median of the posterior on the network matched-filter SNRs obtained during parameter estimation for each segment. The black line in Fig. 1 marks what we consider to be “resolved” segments with $\text{SNR} > 8$, and thus more than 99.7% of segments (95.5% of mergers) are unresolved. However, in the next section, we impose varying cuts based on SNR to study how excluding different segments of the population impacts the detection of the SGWB, thus varying our definition of a resolved segment.

3. WHICH SIGNAL-TO-NOISE RATIOS CONTRIBUTE INFORMATION TO THE TBS?

To understand whether the weakest mergers contribute information to the detection of the SGWB via the duty cycle constraint obtained through the TBS, we calculate the posterior on the duty cycle while replacing noise segments with signal segments and vice versa, in order of ascending SNR. By systematically excluding segments of our population based on their SNR, we can determine how the exclusion affects the posterior on the duty cycle and thus which merger SNRs contribute to the information the TBS obtains. For this part of the study, we down-select 20000 analysis segments from our total population, so that the remaining segments can be used for replacement. We begin with 20000 noise segments and randomly replace these with signal segments with SNRs below the variable threshold $\text{SNR}_{\text{max}}^S$. The first threshold ($\text{SNR}_{\text{max}}^S = 0$) corresponds to only noise segments included in the population, $\xi = 0$, and the final ($\text{SNR}_{\text{max}}^S = 40$) to our true value of $\xi = 0.05$, as the highest SNR of a segment in the population is 38.93. At each threshold, we calculate the ξ posterior, as shown

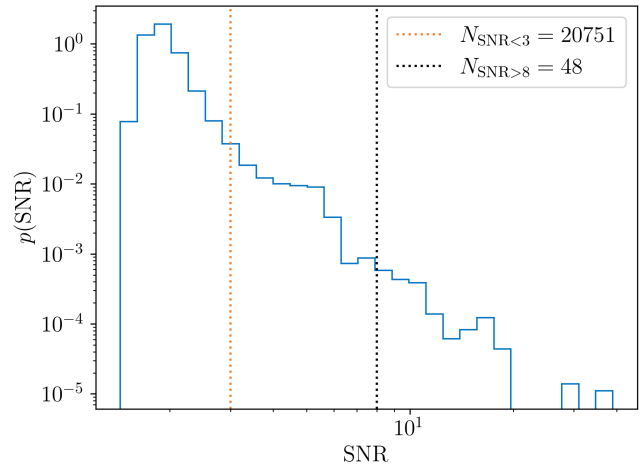


Figure 1. Histogram of the median of the posterior on the network matched filter SNRs for the full dataset with $N = 21600$ segments. The dotted vertical orange line at $\text{SNR} = 3$ is labeled with the number of segments with SNRs below this threshold, 20751, which is $\sim 96\%$ of the total dataset. The dotted vertical black line at $\text{SNR} = 8$ is labeled with the number of segments with SNRs above this threshold, 48, which is $\sim 0.2\%$ of the total dataset.

in the left panel of Fig. 2. We find that when replacing noise segments with signal segments with $\text{SNR} < 7$, we can measure a non-zero duty cycle with $> 99.99\%$ credibility. Because the posterior first excludes $\xi = 0$ with such significance only when segments with SNRs this high are included in the analysis, we conclude that signals with $\text{SNR} < 7$ do not provide sufficient information to definitively detect the SGWB with the TBS, at least with this amount of data.

We next perform the same analysis as above, but now beginning with 19000 noise segments and 1000 signal segments for a population with $\xi = 0.05$. We replace signal segments with SNR below a given threshold with noise segments, until the population contains only noise segments. The right panel of Fig. 2 shows that when we replace signal segments with $\text{SNR} < 6$ with noise segments, there is still significant support for $\xi = 0.05$. Only when we replace signal segments with $\text{SNR} < 7$ out of the population do we measure a duty cycle that excludes $\xi = 0.05$ with $> 97.9\%$ credibility. As we replace signal segments of even higher SNRs with noise, the posterior peaks closer to $\xi = 0$.

Taken together, these results would suggest that BBH mergers with $\text{SNR} \gtrsim 7$ dominate the information obtained using the TBS, and that weaker signals do not contribute any information to the detection of the SGWB. However, the procedure for systematically omitting certain segments from the analysis is not equipped to handle selection thresholds imposed on our

population. This means that the posteriors shown in Fig. 2 are formally biased. We demonstrate how to correct this bias below.

3.1. Incorporating Selection Effects

To correct our likelihood calculation for excluding certain events using SNR cutoffs, we must take into account selection effects, the probability that a merger with specific binary parameters is detectable. The likelihood for a single segment given ξ and a detection threshold is given by renormalizing Eq. 5 (Talbot 2021),

$$\mathcal{L}(d_i|\xi, \text{det}) = \frac{1}{C(\xi)} [\xi \mathcal{L}(d_i|S) + (1 - \xi) \mathcal{L}(d_i|N)]. \quad (6)$$

The likelihood must be normalized when integrating over all detectable data realizations,

$$1 = \int_{d_{\text{det}}} \mathcal{L}(d_i|\xi, \text{det}) dd, \quad (7)$$

$$C(\xi) = \int_{d_{\text{det}}} [\xi \mathcal{L}(d_i|S) + (1 - \xi) \mathcal{L}(d_i|N)] dd. \quad (8)$$

We can simplify the right-hand side by defining two new parameters,

$$\alpha = \int_{d_{\text{det}}} \mathcal{L}(d_i|S) dd, \quad \beta = \int_{d_{\text{det}}} \mathcal{L}(d_i|N) dd, \quad (9)$$

each representing the fraction of astrophysical or noise events that pass a detection threshold (Vitale et al. 2022), such that

$$\alpha \equiv \frac{N_S^{\uparrow\downarrow}}{N_S}, \quad \beta \equiv \frac{N_N^{\uparrow\downarrow}}{N_N}, \quad (10)$$

$$C(\xi) = \xi \alpha + (1 - \xi) \beta, \quad (11)$$

where N_S is the number of signal segments, N_N the number of noise segments, and the $\uparrow\downarrow$ superscript denotes whether the cutoff is above or below a SNR threshold. Normalizing Eq. 5 by $C(\xi)$,

$$\mathcal{L}(d|\xi, \text{det}) = \prod_i \frac{1}{C(\xi)} [\xi \mathcal{Z}_S^i + (1 - \xi) \mathcal{Z}_N^i], \quad (12)$$

we obtain the correction to the likelihood accounting for selection bias, allowing us to reanalyze the population with various SNR thresholds.

We begin by imposing a threshold on the maximum SNR of segments included in the analysis, omitting the loudest signals. The top row of Fig. 3 shows that when only including segments with SNR < 3, 4, 5, the posterior on the duty cycle peaks at $\xi = 0$, meaning that we do not detect the SGWB with only information contained within these sub-threshold populations of BBH

mergers. However, the ξ posteriors in the second row of Fig. 3 with SNR < 6, 7, 8 peak away from $\xi = 0$, showing support for the detection of the SGWB. While the posterior calculated using our full simulated dataset (in white) for SNR < 6 peaks away from zero but with only marginal support at $\xi = 0.05$, many of the bootstrapped posterior realizations (in color) have significant support at the true value.

We postulate that this bias in the ξ posterior that remains when excluding segments with SNR < 7 in the analysis even when using the likelihood accounting for selection effects is caused by a subtle breakdown in the statistical assumptions underlying the Bayesian TBS method. The uncertainty on the signal and noise evidences obtained by the stochastic sampler likely overwhelms the precision required to distinguish signals from noise at such low SNRs. We thus find that there is insufficient information to definitively detect the SGWB when only analyzing segments with SNR < 5. However, we find growing evidence for a background in a population with segments with only SNR < 6, markedly below current standard detection statistics for individual events corresponding to SNR \gtrsim 8–12.

Next, we impose a threshold on the minimum SNR of segments included in the analysis, omitting the quietest segments. The third row of Fig. 3 shows that when we include segments with SNR > 3, 4, 5 in our analysis, we recover the true duty cycle. There is a slight bias towards higher duty cycles in these posteriors, likely because the values of α and β in the renormalization for selection effects are calculated from a set of finite BBH mergers, meaning there is some inherent uncertainty from the randomness of the merger parameters generated. When we exclude the portion of the population with SNR < 6 (bottom left of Fig. 3), the width of the posterior on ξ increases significantly. The final two posteriors calculated with thresholds of SNR > 7, 8 are extremely broad without definitive peaks because $\beta \sim \mathcal{O}(10^{-4}) \approx 0$. As discussed above, this is due to the constraints of a finite population size, as given a large enough population, some Gaussian noise would in fact “pass” even these high detection thresholds of SNR > 7, 8. These results suggest that the uncertainty in the measurement of the SGWB increases as we exclude lower SNR events.

While we find that the width of the posterior on the duty cycle increases with the minimum SNR threshold, this effect could be dominated by the reduced size of the analyzed dataset by imposing increasingly stringent thresholds. To disentangle this effect, we randomly down-sample the full dataset to include the same total number of segments in the analysis, including both

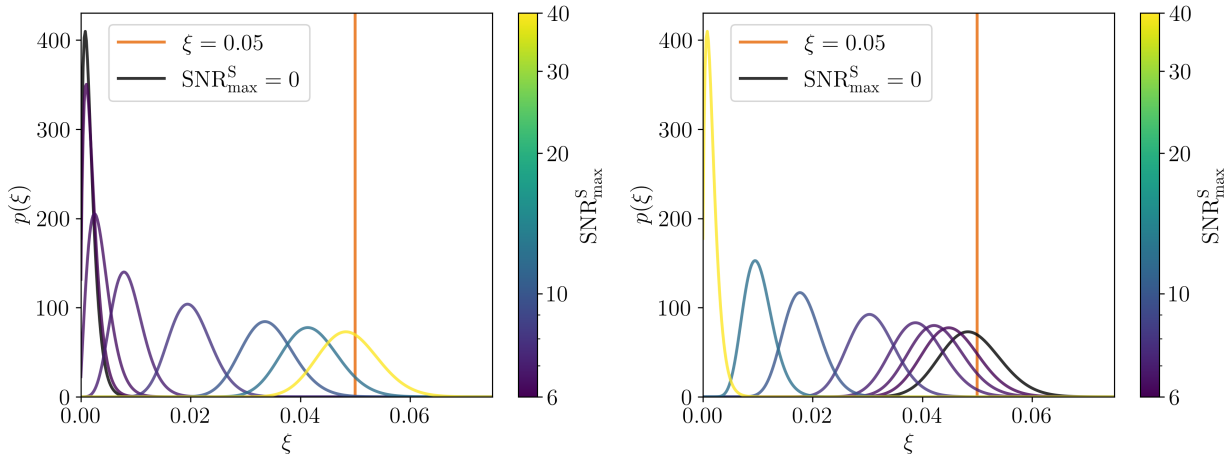


Figure 2. *Left:* Posterior on the duty cycle for a population beginning with only noise segments, and replacing them with signal segments with $\text{SNR} < \text{SNR}_{\text{max}}^{\text{S}}$, for $\text{SNR}_{\text{max}}^{\text{S}} = \{0, 6, 6.5, 7, 8, 10, 12, 40\}$ until $\xi = 0.05$ (shown in orange). Note that all signal segments have $\text{SNR} \leq 40$. *Right:* Posterior on the duty cycle beginning with a population with $\xi = 0.05$ and replacing signal segments with $\text{SNR} < \text{SNR}_{\text{max}}^{\text{S}}$ with noise segments until $\xi = 0.0$.

signal and noise segments, as the threshold varies. We use $N = 54$, corresponding to the number of segments with $\text{SNR} > 7.5$. For each SNR threshold, we bootstrap 200 realizations of $N = 54$ segments passing the threshold, enforcing that the resulting duty cycle is the same as that obtained by applying that threshold to the full dataset. We then calculate the ξ posterior and its 90% credible interval width, CI_{90} , for each realization but note that not all realizations are independent, given the finite size of the dataset.

Fig. 4 shows the ξ posterior CI_{90} as a function of the minimum SNR threshold imposed on the population. The shaded region shows the 50% credible interval for the calculated CI_{90} values across the 200 dataset realizations for each threshold. We choose to plot the 50% credible interval because we only have two independent realizations of $N = 54$ segments at the largest SNR shown on the x-axis, $\text{SNR} = 5.8$, such that

$$\text{CI}_{50} = 1 - 1/N_{\text{ind}} = 1 - N_{\text{SNR} > 7.5} / N_{\text{SNR} > 5.8}. \quad (13)$$

While the ξ posteriors remain similarly precise while including segments with $\text{SNR} > 3$ as with $\text{SNR} > 5$, the uncertainty grows by more than a factor of three when we only include segments with $\text{SNR} > 5.8$. Hence, we conclude that the width of the duty cycle posterior increases as segments with $\text{SNR} \approx 5$ are excluded from the analysis, even when keeping the size of the analyzed dataset constant. This result and results from the selection effects analyses in Fig. 3 demonstrate that the dominant information obtained by the TBS on the detection of the SGWB via the ξ posterior comes from segments with $\text{SNR} \sim 5-7$, just below the threshold for individual-event detection, in qualitative agreement with the results of Renzini et al. (2024).

4. CONSTRAINING THE BBH MERGER REDSHIFT DISTRIBUTION

The results presented in Section 3 imply that the weakest signals do not contribute significant information to the detection of the SGWB with the TBS, but we are also interested in determining whether they contribute information to the characterization of the BBH population sourcing the background. To this end, we analyze the same population described in Section 2 but now simultaneously infer the duty cycle and the BBH population properties, focusing on the redshift distribution. Critically, as of the latest GW catalog, GWTC-3 (Abbott et al. 2023a), no BBH mergers have been individually resolved beyond the peak of star formation at $z_p \approx 1.9$. Thus, demonstrating a constraint on the merger redshift distribution at larger redshifts would show that we can learn about the properties of BBH mergers beyond the peak of star formation without detecting these sources individually at current sensitivities.

4.1. Hierarchical Bayesian Inference

We adapt the likelihood in Eq. 5 to allow for a flexible population model rather than assuming the fixed model used as the prior for the individual-event parameter estimation (Smith et al. 2020)

$$\mathcal{L}(\{d\}|\Lambda, \xi) = \prod_i^n [\xi \mathcal{L}(d_i|\Lambda, S) + (1 - \xi) \mathcal{Z}_N^i], \quad (14)$$

where the likelihood of a single segment of data given the hyper-parameters, Λ , and the signal hypothesis, S , is

$$\mathcal{L}(d_i|\Lambda, S) = \int \mathcal{L}(d_i|\theta, S) \pi(\theta|\Lambda) d\theta. \quad (15)$$

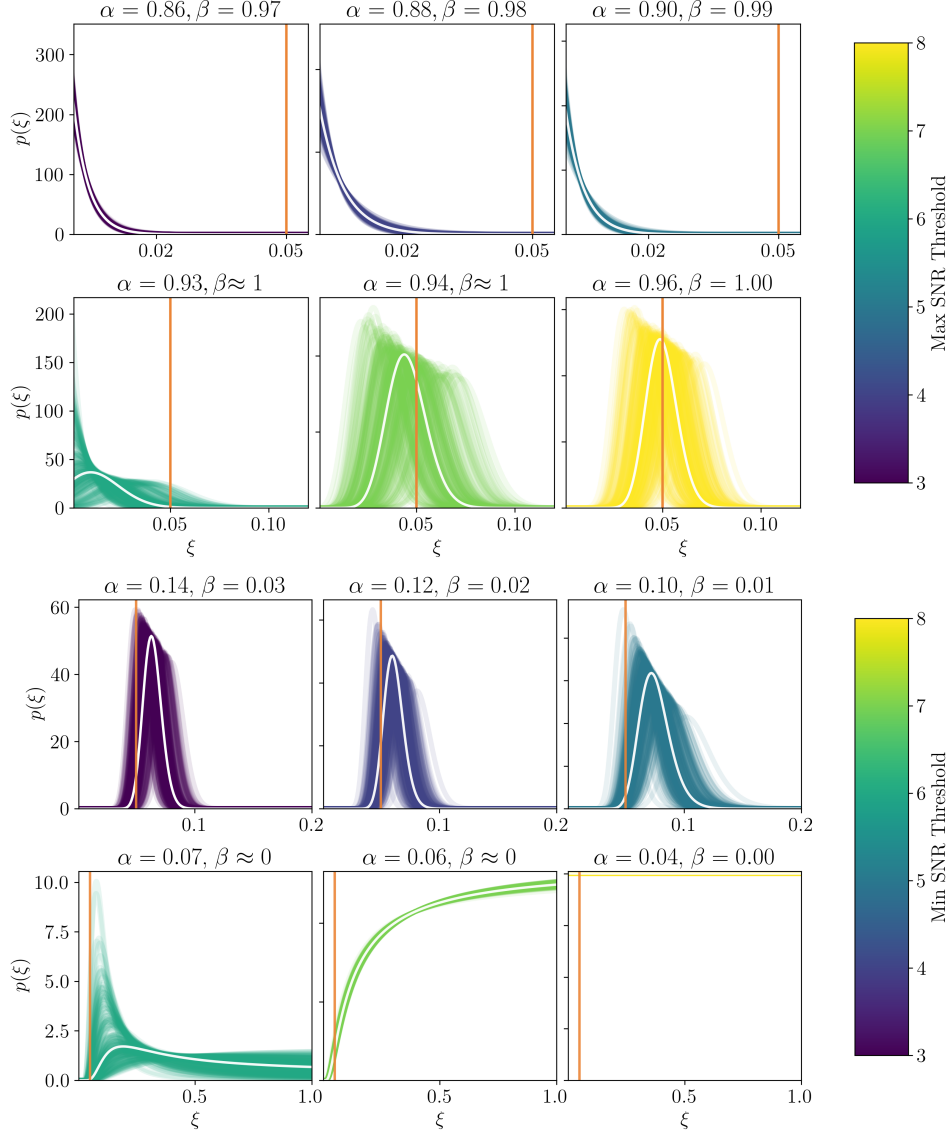


Figure 3. Posterior on the duty cycle with selection effects taken into account calculated on the population while only including segments with SNRs below the maximum SNR threshold in the top two rows of the grid, and only including segments with SNRs above the minimum SNR threshold in the bottom two rows of the grid. The colored lines show the posterior on the duty cycle for 200 bootstrapped realization of the dataset while holding the duty cycle of the segments that pass that threshold fixed. The white lines show the posterior calculated with the full population, and the true value of the duty cycle is shown in orange, $\xi = 0.05$. The α, β values shown above each plot are the fractions of signal and noise segments, respectively, that pass the selection criteria (see Eq. 10).

The likelihood in Eq. 15 is typically calculated using Monte Carlo (MC) integration to “recycle” the binary parameter posteriors obtained under the individual-event parameter estimation prior so that Eq. 14 becomes

$$\mathcal{L}(\{d\}|\Lambda, \xi) = \prod_i^n \left[\frac{\xi}{m} \sum_j^m \frac{Z_S^i \pi(\theta_{ij}|\Lambda)}{\pi(\theta_{ij}|\Lambda_0)} + (1 - \xi) Z_N^i \right] \quad (16)$$

with $\{\kappa, \gamma, z_p\} \in \Lambda$ and $\theta = z$ for simultaneous inference of the redshift distribution with the duty cycle. The

index j indicates the individual-event posterior sample for θ , and Λ_0 represents the shape of the binary parameter priors used for individual-segment parameter estimation. However, we encountered challenges in using the MC integration technique due to the size of our population, as the uncertainty in the integral scales with the number of analyzed segments in the population (Talbot & Golomb 2023).

In our population with 21600 total segments, the large uncertainties artificially inflate the likelihood at certain points in parameter space, leading to biased posteriors.

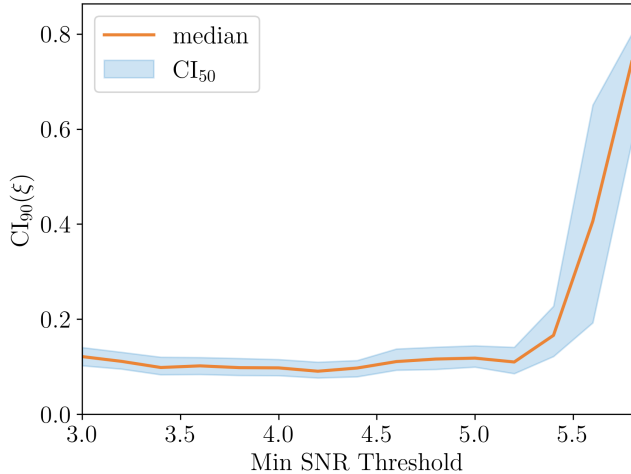


Figure 4. Median 90% credible interval of 200 bootstrapped posterior calculations on ξ in orange, with the shaded blue showing the 50% credible interval of the median CI_{90} s as a function of the minimum SNR threshold imposed. Each bootstrapped posterior is calculated by randomly down-sampling with replacement a set of the segments whose SNRs are greater than the thresholds such that all posterior calculations include the same number of total segments.

Parameter Λ	True value	Hyper Prior $\pi(\Lambda)$
ξ	0.05	Uniform(0, 1)
κ	5.6	Uniform(-2, 10)
γ	2.7	Uniform(-2, 10)
z_p	1.9	Uniform(0.5, 3.28)

Table 1. Hyper-parameter Priors

ξ is the astrophysical duty cycle, κ describes the slope of the redshift distribution shape at high z , γ describes the slope of the redshift distribution shape at low z , and z_p is the peak of redshift distribution.

We find that ξ , γ , and z_p are biased towards larger values, while κ is biased towards smaller values. We initially attempted to circumvent this issue by replacing the MC integral with a trapezoidal integral, but the various density estimation techniques we used to obtain continuous representations of the individual-event redshift posteriors were insufficiently accurate to obtain unbiased hierarchical inference results for our full population (see Appendix A for more details). Instead, we use likelihood reweighting (e.g., Payne et al. 2019) to map the posterior on ξ given a fiducial population model, $p(\xi|\{d\}, \Lambda_0)$, to the likelihood given a generic set

of hyper-parameters, Λ , marginalizing over ξ :

$$\mathcal{L}(\{d\}|\Lambda) = \int \mathcal{L}(\{d\}|\Lambda, \xi)\pi(\xi)d\xi, \quad (17)$$

$$\mathcal{L}(\{d\}|\Lambda) = \int \frac{\mathcal{L}(\{d\}|\Lambda, \xi)}{\mathcal{L}(\{d\}|\Lambda_0, \xi)} \mathcal{Z}_0 p(\xi|\{d\}, \Lambda_0) d\xi, \quad (18)$$

where in the last line we have used Bayes' theorem to replace the product of the likelihood and prior with the product of the posterior and the evidence obtained using the fiducial hyper-parameter values. Converting the integral into a sum over posterior samples, the total likelihood is

$$\mathcal{L}(\{d\}|\Lambda) = \frac{\mathcal{Z}_0}{\ell} \sum_k \frac{\mathcal{L}(\{d\}|\Lambda, \xi_k)}{\mathcal{L}(\{d\}|\Lambda_0, \xi_k)} \quad (19)$$

where $\mathcal{L}(\{d\}|\Lambda, \xi_k)$ is given by Eq. 16. Once posterior samples are obtained for Λ , the updated ξ posterior can be reconstructed in post-processing:

1. For each posterior sample Λ_k , we calculate $\mathcal{L}_k(\{d\}|\xi) = \mathcal{L}(\{d\}|\Lambda_k, \xi)$ over a grid of ξ values.
2. Given the choice of ξ prior assumed during the initial sampling from $p(\xi|\{d\}, \Lambda_0)$, we calculate the ξ posterior,

$$p_k(\xi|\{d\}) \propto \mathcal{L}_k(\{d\}|\xi)\pi(\xi). \quad (20)$$

3. Using inverse transform sampling, we generate a random sample from this posterior associated with that Λ_k sample.
4. Repeat this procedure for each Λ_k .

We note that likelihood reweighting is only effective in our use case if the posterior obtained on ξ using the fiducial population model, $p(\xi|\{d\}, \Lambda_0)$, has significant overlapping support with the final posterior obtained under the flexible population model, $p(\xi, \Lambda|\{d\})$. This is easier to guarantee in a simulation, as we chose Λ_0 to be equal to the true values of Λ , which is not possible for real data. However, a similar approach could be taken for real data by choosing Λ_0 to match the maximum likelihood hyper-parameters inferred for the resolved population, which we expect will be similar to the unresolved population, at least at small redshifts. We leave further exploration of the applicability of this likelihood reweighting technique for simultaneous hierarchical inference at scale using real data to future work.

4.2. Results

Fig. 5 shows the posterior on the redshift distribution obtained in the analysis of the entire population compared to the simulated Madau-Dickinson redshift distribution from which the population was drawn. We are

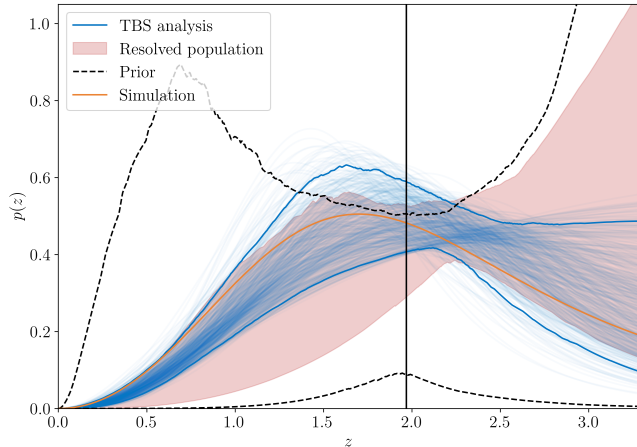


Figure 5. Inferred redshift distribution obtained using hierarchical inference. In blue thin lines are posteriors on the redshift distribution calculated using the Madau-Dickinson parameterization for individual hyper-parameter posterior samples. The solid blue lines bound the CI_{90} for the full population analysis, the orange solid line is the true population prior Madau-Dickinson distribution, and the dashed black lines are the CI_{90} prior bound. The shaded red region is the CI_{90} for the analysis including only resolved segments and taking into account selection effects, and the solid black vertical line at $z = 1.97$ marks the redshift of the farthest signal in the population with $\text{SNR} > 8$.

able to recover the shape of the simulated redshift distribution of BBH mergers out to redshifts beyond those where resolved events are individually detected. Crucially, the Bayesian TBS enables us to constrain the posterior on the redshift hyper-parameters significantly not only relative to the prior but also relative to a standard hierarchical analysis limited to the resolved population with $\text{SNR} > 8$ accounting for selection effects with fixed $\xi = 1$ (red shading). By not distinguishing between a foreground and background, we find that the unresolved population must be contributing to the constraint on the redshift distribution at high redshifts. The narrowing of the constraint on the shape of the redshift distribution seen at $z \approx 2$ is due to the parameterization used, as the prior is also narrower. The parameterization also causes the lower bound of the TBS posterior on the redshift distribution to fall below the lower bound of the resolved population posterior at high redshifts ($z \gtrsim 2$). The merger rate at large redshifts inferred with the resolved analysis falls as quickly as the parameterized form allows given the increased support for lower merger rates at small redshifts relative to the analysis including unresolved mergers.

When analyzing the simulated data with the above-described likelihood reweighting method for hierarchical inference on the redshift distribution and the duty cycle,

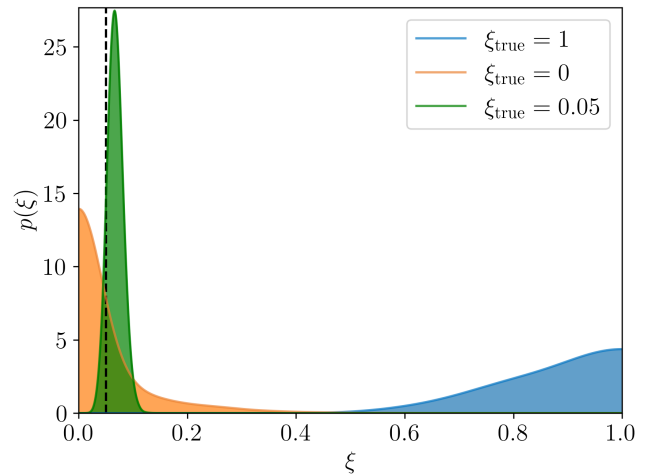


Figure 6. Posteriors on the duty cycle from hierarchical inference with all segments in green demonstrating that the TBS is unbiased, only noise segments in orange demonstrating that the TBS is safe, and only signal segments in blue demonstrating that the TBS is effective.

we test to ensure that the TBS is safe, unbiased, and effective. As shown in the ξ posterior comparison plot in Fig. 6, we find that all three are true: When only Gaussian noise segments are analyzed (orange), we find that the posterior on ξ peaks at 0, meaning the method is safe. When the entire population is analyzed (green), we find that the posterior on ξ has significant support at the true value of $\xi = 0.05$, meaning the method is unbiased. Finally, when analyzing only the signal subset of the population (blue), we find the posterior peaks at 1.0 and rules out $\xi = 0$, meaning the method is effective at detecting the SGWB.

While we have chosen an artificially inflated value of the duty cycle to curtail the computational cost of our simulation, we want to demonstrate the robustness of our constraints on the redshift distribution for a more realistic choice of ξ . Fig. 7 shows that the posteriors for the individual hyper-parameters that describe the redshift distribution are consistent when analyzing just signal segments, i.e., $\xi_{\text{true}} = 1$, all segments but fixing $\xi_{\text{true}} = 0.05$, and when analyzing the whole population with the method described above. This means that varying the true value of ξ does not affect our ability to constrain the redshift distribution. Imperfect knowledge of ξ (simultaneous inference) similarly does not affect the constraints obtained on the population distribution. As such, the constraints on the redshift distribution that we demonstrate for our simulated population can be obtained with any amount of data required for the detection of 48 resolved, high-mass BBH at O4 sensitivity,

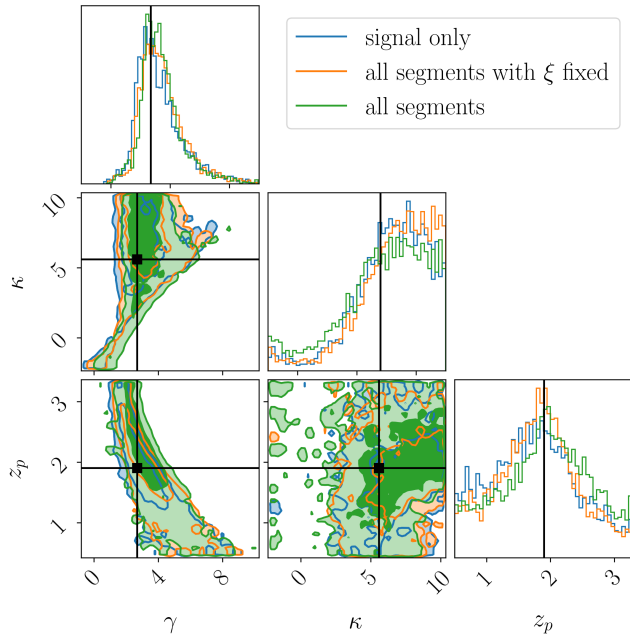


Figure 7. Comparison corner plot of the posteriors on the redshift distribution hyper-parameters from hierarchical inference using all segments in green, only signal segments in blue, and all segments with the duty cycle fixed to the true value in orange. The darker region is the 90% credible region, and the lighter is the 50% credible region. The black lines indicate the true values of the hyper-parameters.

whether that corresponds to one day as in our simulation, or more realistically $\mathcal{O}(\text{months})$.

5. CONCLUSIONS

In this work, we seek to determine where the information driving the detection of the SGWB using the Bayesian TBS comes from and whether the farthest, unresolved BBH mergers contribute to the constraint on the merger redshift distribution at large redshifts beyond the peak of star formation. We begin by imposing SNR thresholds to determine which segments contribute to the constraint on the duty cycle, both ignoring and accounting for selection effects. Our results demonstrate that signal segments with SNRs between ~ 5 – 7 dominate the information on the detection of the SGWB that is accessible with the TBS, in qualitative agreement with [Renzini et al. \(2024\)](#), which instead uses a Fisher information matrix to directly calculate contributions to the detection of the SGWB.

We then expand upon the work of [Smith et al. \(2020\)](#) to use hierarchical Bayesian inference to constrain the merger redshift distribution simultaneously with the duty cycle. With one day of simulated GW data at O4 sensitivity, we show that while weak segments do not contribute significantly to the measurement of the

duty cycle obtained with the TBS, the individually unresolved segments *do* constrain the posterior on the redshift distribution at redshifts beyond the peak of star formation and beyond where any signals are resolved with current detector sensitivities. The constraints on the redshift distribution are not only informative relative to the prior but also relative to an analogous hierarchical analysis on resolved events only.

While our results also show that the value of the duty cycle does not impact the ability to infer the redshift distribution hyper-parameters, it is important to recognize that our analysis is using a significantly inflated value of ξ compared to the value expected astrophysically ([Smith & Thrane 2018](#)). We leave an analysis that uses a more realistic value of $\xi \sim \mathcal{O}(10^{-4})$ to future work. We also note that our analysis is performed on simulated frequency-domain data, and there are non-trivial modifications that would be needed to use the TBS with real time-domain data. One such factor is the uncertainty in the estimated power spectral density of real data; another is the off-diagonal terms that appear in the likelihood noise covariance matrix that are ignored in frequency-domain simulations due to assumed periodic boundary conditions for the noise that lead to a diagonal matrix ([Talbot & Thrane 2020](#); [Talbot et al. 2021](#); [Kou et al. 2025](#)). Finally, while we only infer the BBH merger redshift distribution, an extension of this work should simultaneously infer the mass and spin distributions alongside the redshift, as their posteriors may be correlated, leading to an increase in the uncertainty in the redshift distribution inference.

In addition to fitting both the mass and spin distributions, in future work, we will explore using a non-parametric redshift distribution model such that the priors and assumed parameterization have a smaller impact on the shape of the posterior. As shown in [Fig. 5](#), the prior causes the posteriors on the redshift to narrow right after $z \approx 2$, whereas this would not necessarily be the case given a non-parametric redshift distribution model. Finally, an important future extension of our work is a direct comparison of the redshift distribution constraint obtained with the TBS to the method described in [Callister et al. \(2020\)](#) that analyzes the foreground and background separately, as opposed to our threshold-less analysis.

The authors thank Colm Talbot and Vicky Kalogera for insightful suggestions and discussions and Saleem Muhammed for providing helpful comments during internal LVK document review. This material is based upon work supported by NSF’s LIGO Laboratory which is a major facility fully funded by the National Science Foundation. LIGO was constructed by the Califor-

nia Institute of Technology and Massachusetts Institute of Technology with funding from the National Science Foundation and operates under cooperative agreement PHY-0757058. S.B. is supported by NASA through the NASA Hubble Fellowship grant HST-HF2-51524.001-A awarded by the Space Telescope Science Institute, which is operated by the Association of Universities for Research in Astronomy, Inc., for NASA, under contract NAS5-26555. N.B. is supported by NSF grant PHY-

2207945 and through a NASA grant awarded to the Illinois/NASA Space Grant Consortium. Any opinions, findings, conclusions, or recommendations expressed in this material are those of the authors and do not necessarily reflect the views of NASA. The authors are grateful for computational resources provided by the Caltech LIGO Laboratory supported by NSF PHY-0757058 and PHY-0823459. This paper carries LIGO document number LIGO-P2500381.

REFERENCES

- Aasi, J., et al. 2015, *Class. Quant. Grav.*, 32, 074001
- Abbott, B. P., et al. 2018a, *Living Rev. Rel.*, 21, 3
- 2018b, *Phys. Rev. Lett.*, 120, 091101
- 2018c, *Phys. Rev. Lett.*, 120, 201102
- 2022, Noise curves used for Simulations in the update of the Observing Scenarios Paper,
<https://dcc.ligo.org/LIGO-T2000012/public>, ,
- Abbott, R., et al. 2021a, *Phys. Rev. D*, 104, 022004
- 2021b, *Phys. Rev. D*, 104, 022005
- 2023a, *Phys. Rev. X*, 13, 041039
- 2023b, *Phys. Rev. X*, 13, 011048
- Acernese, F., et al. 2015, *Class. Quant. Grav.*, 32, 024001
- Akutsu, T., et al. 2021, *PTEP*, 2021, 05A101
- Allen, B., & Romano, J. D. 1999, *Phys. Rev. D*, 59, 102001
- Ashton, G., et al. 2019, *Astrophys. J. Suppl.*, 241, 27
- Aso, Y., Michimura, Y., Somiya, K., et al. 2013, *Phys. Rev. D*, 88, 043007
- Biscoveanu, S., Isi, M., Vitale, S., & Varma, V. 2021, *Phys. Rev. Lett.*, 126, 171103
- Callister, T., Fishbach, M., Holz, D., & Farr, W. 2020, *Astrophys. J. Lett.*, 896, L32
- Callister, T., Sammut, L., Qiu, S., Mandel, I., & Thrane, E. 2016, *Phys. Rev. X*, 6, 031018
- Callister, T., Biscoveanu, A. S., Christensen, N., et al. 2017, *Phys. Rev. X*, 7, 041058
- Callister, T. A., & Farr, W. M. 2024, *Phys. Rev. X*, 14, 021005
- Callister, T. A., Miller, S. J., Chatzioannou, K., & Farr, W. M. 2022, *Astrophys. J. Lett.*, 937, L13
- Christensen, N. 1992, *Phys. Rev. D*, 46, 5250
- Coughlin, M. W., et al. 2016, *Class. Quant. Grav.*, 33, 224003
- Cousins, B., Schumacher, K., Chung, A. K.-W., et al. 2025, [arXiv:2503.01997](https://arxiv.org/abs/2503.01997)
- De Lillo, F., & Suresh, J. 2024, *Phys. Rev. D*, 109, 103013
- Drasco, S., & Flanagan, E. E. 2003, *Phys. Rev. D*, 67, 082003
- Edelman, B., Doctor, Z., Godfrey, J., & Farr, B. 2022, *Astrophys. J.*, 924, 101
- Edelman, B., Farr, B., & Doctor, Z. 2023, *Astrophys. J.*, 946, 16
- Essick, R., & Fishbach, M. 2024, *Astrophys. J.*, 962, 169
- Farr, W. M., Gair, J. R., Mandel, I., & Cutler, C. 2015, *Phys. Rev. D*, 91, 023005
- Ferraiuolo, S., Mastrogiovanni, S., Escoffier, S., & Kajfasz, E. 2025, [arXiv:2503.14686](https://arxiv.org/abs/2503.14686)
- Fishbach, M., & Holz, D. E. 2017, *Astrophys. J. Lett.*, 851, L25
- Fishbach, M., Doctor, Z., Callister, T., et al. 2021, *Astrophys. J.*, 912, 98
- Gaebel, S. M., Veitch, J., Dent, T., & Farr, W. M. 2019, *Mon. Not. Roy. Astron. Soc.*, 484, 4008
- Galadage, S., et al. 2021, *Astrophys. J. Lett.*, 921, L15, [Erratum: *Astrophys. J. Lett.* 936, L18 (2022), Erratum: *Astrophys. J.* 936, L18 (2022)]
- Hannam, M., Schmidt, P., Bohé, A., et al. 2014, *Phys. Rev. Lett.*, 113, 151101
- Himemoto, Y., Nishizawa, A., & Taruya, A. 2023, *Phys. Rev. D*, 107, 064055
- Himemoto, Y., & Taruya, A. 2019, *Phys. Rev. D*, 100, 082001
- Hoy, C., & Raymond, V. 2021, *SoftwareX*, 15, 100765
- Janssens, K., et al. 2023, *Phys. Rev. D*, 107, 022004
- Kou, X.-X., Fragione, G., & Mandic, V. 2024, *Phys. Rev. D*, 109, 123036
- Kou, X.-X., Saleem, M., Mandic, V., Talbot, C., & Thrane, E. 2025, [arXiv:2506.14179](https://arxiv.org/abs/2506.14179)
- Lalleman, M., Turbang, K., Callister, T. A., & Van Remortel, N. 2024, *PoS, EPS-HEP2023*, 088
- Lawrence, J., Turbang, K., Matas, A., et al. 2023, *Phys. Rev. D*, 107, 103026
- LIGO Scientific Collaboration. 2024, LIGO/Virgo/KAGRA Public Alerts,
<https://gracedb.ligo.org/superevents/public/O4/>, ,
- Loredo, T. J. 2004, *AIP Conf. Proc.*, 735, 195

- Madau, P., & Dickinson, M. 2014, *Ann. Rev. Astron. Astrophys.*, 52, 415
- Mandel, I., Farr, W. M., & Gair, J. R. 2019, *Mon. Not. Roy. Astron. Soc.*, 486, 1086
- Mandic, V., Thrane, E., Giampanis, S., & Regimbau, T. 2012, *Phys. Rev. Lett.*, 109, 171102
- Martinovic, K., Badger, C., Sakellariadou, M., & Mandic, V. 2021, *Phys. Rev. D*, 104, L081101
- Matas, A., & Romano, J. D. 2021, *Phys. Rev. D*, 103, 062003
- Messenger, C., & Veitch, J. 2013, *New J. Phys.*, 15, 053027
- Meyers, P. M., Martinovic, K., Christensen, N., & Sakellariadou, M. 2020, *Phys. Rev. D*, 102, 102005
- Mould, M., Gerosa, D., Broekgaarden, F. S., & Steinle, N. 2022, *Mon. Not. Roy. Astron. Soc.*, 517, 2738
- Mukherjee, S., & Silk, J. 2020, *Mon. Not. Roy. Astron. Soc.*, 491, 4690
- . 2021, *Mon. Not. Roy. Astron. Soc.*, 506, 3977
- Payne, E., Talbot, C., & Thrane, E. 2019, *Phys. Rev. D*, 100, 123017
- Payne, E., & Thrane, E. 2023, *Phys. Rev. Res.*, 5, 023013
- Price-Whelan, A. M., et al. 2022, *Astrophys. J.*, 935, 167
- Ray, A., Magaña Hernandez, I., Mohite, S., Creighton, J., & Kapadia, S. 2023, *Astrophys. J.*, 957, 37
- Regimbau, T. 2011, *Res. Astron. Astrophys.*, 11, 369
- Renzini, A. I., Callister, T., Chatziioannou, K., & Farr, W. M. 2024, *Phys. Rev. D*, 110, 023014
- Renzini, A. I., & Golomb, J. 2024, *Astron. Astrophys.*, 691, A238
- Rinaldi, S., & Del Pozzo, W. 2021, *Mon. Not. Roy. Astron. Soc.*, 509, 5454
- Romano, J. D., & Cornish, N. J. 2017, *Living Rev. Rel.*, 20, 2
- Romero-Shaw, I. M., et al. 2020, *Mon. Not. Roy. Astron. Soc.*, 499, 3295
- Rosado, P. A. 2011, *Phys. Rev. D*, 84, 084004
- Roulet, J., Chia, H. S., Olsen, S., et al. 2021, *Phys. Rev. D*, 104, 083010
- Safarzadeh, M., Biscoveanu, S., & Loeb, A. 2020, *Astrophys. J.*, 901, 137
- Sah, M. R., & Mukherjee, S. 2024, *Mon. Not. Roy. Astron. Soc.*, 527, 4100
- Smith, R., & Thrane, E. 2018, *Phys. Rev. X*, 8, 021019
- Smith, R. J. E., Talbot, C., Hernandez Vivanco, F., & Thrane, E. 2020, *Mon. Not. Roy. Astron. Soc.*, 496, 3281
- Smith, R. J. E., Talbot, C., Hernandez Vivanco, F., & Thrane, E. 2020, *MNRAS*, 496, 3281
- Somiya, K. 2012, *Class. Quant. Grav.*, 29, 124007
- Speagle, J. S. 2020, *Monthly Notices of the Royal Astronomical Society*, 493, 3132
- Talbot, C. 2021, *Population inference with marginal events: an update*, Tech. rep., <https://dcc.ligo.org/LIGO-T2100147>
- Talbot, C., & Golomb, J. 2023, *Mon. Not. Roy. Astron. Soc.*, 526, 3495
- Talbot, C., & Thrane, E. 2018, *Astrophys. J.*, 856, 173
- . 2020, *Phys. Rev. Res.*, 2, 043298
- . 2022, *Astrophys. J.*, 927, 76
- Talbot, C., Thrane, E., Biscoveanu, S., & Smith, R. 2021, *Phys. Rev. Res.*, 3, 043049
- Thrane, E. 2013, *Phys. Rev. D*, 87, 043009
- Thrane, E., Christensen, N., & Schofield, R. 2013, *Phys. Rev. D*, 87, 123009
- Thrane, E., Christensen, N., Schofield, R. M. S., & Effler, A. 2014, *Phys. Rev. D*, 90, 023013
- Thrane, E., & Talbot, C. 2019, *Publications of the Astronomical Society of Australia*, 36, e010
- Tiwari, V., & Fairhurst, S. 2021, *Astrophys. J. Lett.*, 913, L19
- Tong, H., Galaudage, S., & Thrane, E. 2022, *Phys. Rev. D*, 106, 103019
- Turbang, K., Lalleman, M., Callister, T. A., & van Remortel, N. 2024, *Astrophys. J.*, 967, 142
- Vitale, S., Gerosa, D., Farr, W. M., & Taylor, S. R. 2022, in *Handbook of Gravitational Wave Astronomy*, ed. C. Bambi, S. Katsanevas, & K. D. Kokkotas (Springer), 45
- Zhu, X.-J., Howell, E., Regimbau, T., Blair, D., & Zhu, Z.-H. 2011, *Astrophys. J.*, 739, 86
- Zhu, X.-J., Howell, E. J., Blair, D. G., & Zhu, Z.-H. 2013, *Mon. Not. Roy. Astron. Soc.*, 431, 882

APPENDIX

A. DEALING WITH MONTE CARLO INTEGRAL UNCERTAINTY

With 21600 individual-segment redshift posteriors included in our hierarchical analysis, the uncertainty associated with the MC integral in Eq. 16 becomes untractably large, resulting in spuriously large likelihood values at certain points in the parameter space. In particular, we find that the variance in the MC integral is strongly correlated with the inference of the duty cycle and γ and anticorrelated with κ . This leads to a bias towards larger values of ξ, γ and small values of κ , corresponding to redshift distributions that peak strongly at the edge of the allowed redshift range.

We explore several methods to mitigate this bias. The variance in the MC integral can be reduced by increasing the number of samples over which the sum is performed. To generate more samples without repeating the computationally-expensive individual-event parameter estimation step, we can use density estimation to obtain a continuous representation for $p(z|d_i)$ for each segment from which we can draw samples. We first attempt to use a kernel density estimate (KDE) as implemented in PESUMMARY (Hoy & Raymond 2021), which is well-suited to density estimation problems with low dimensionality. We also attempt to fit $p(z|d_i)$ using a three-component Gaussian mixture model (GMM) as implemented in SCIKIT-LEARN, using the CDF mapping proposed in Talbot & Thrane (2022) to avoid edge effects due to sharp cutoffs in the posteriors at the upper edge. The number of components is determined empirically by comparing the performance of the GMM using a variable number of components on a reserved testing subset of the original posterior samples for a few individual events. The performance of the GMM is quantified using the score, or average log-density evaluated over the testing samples.

We then use inverse transform sampling from the posterior density approximated using both the KDE and GMM methods to generate 20000 posterior samples for each event, roughly an order of magnitude more than were produced by the original nested sampling analysis, feeding these new samples to the MC integral in Eq. 16. While the GMM provides an improved fit compared to the KDE, we find that neither method provides a sufficiently accurate representation of the posterior to ensure an unbiased hierarchical inference likelihood. This is demonstrated in Fig. 8, which shows the log likelihood as a function of κ with the other hyper-parameters fixed to their true values for the various likelihood evaluation methods we explore, applied to a population of 500 signal segments. Compared to the likelihood evaluated using a MC integral over the original samples generated by nested sampling shown in red, both the KDE and GMM MC integral likelihood evaluation methods return larger likelihood values at small κ values and smaller likelihood values at large κ , exacerbating the original bias we found using MC integration over the original posterior samples for the full population of 21600 segments.

We also attempt to eschew MC integration altogether, instead using a trapezoidal integral over a grid of redshifts for Eq. 15,

$$\mathcal{L}(d_i|\Lambda) \approx \sum_{j=1}^M \frac{\mathcal{L}(d_i|z_{j-1})\pi(z_{j-1}|\Lambda) + \mathcal{L}(d_i|z_j)\pi(z_j|\Lambda)}{2} \Delta z_j. \quad (\text{A1})$$

where we use Bayes' theorem to replace the single-event likelihood with the ratio of the posterior and the original parameter estimation prior. While performing this gridded integral over the KDE approximation for the individual-event posteriors leads to less hierarchical likelihood bias than the MC integral over samples drawn from the KDE posterior, the bias is not fully ameliorated.

We are only interested in the individual-event likelihoods marginalized over all parameters except for redshift, which are directly derived from the luminosity distance likelihoods given a cosmology. Since we analytically marginalize over luminosity distance during sampling, we can directly reconstruct this likelihood without relying on any density estimation technique and pass this gridded likelihood directly into the trapezoidal integral in Eq. A1. This approach, shown in orange in Fig. 8, yields the least bias in the hierarchical likelihood compared to the MC integral over the original samples. While we find unbiased hierarchical inference results using this method applied to only the signal segments in our population, the analytic likelihood reconstruction is not sufficiently accurate when we begin incorporating noise segments into our analysis, leading to the same kind of bias we found with the MC integral over the original posterior samples applied to our full population.

The most severe bias among the likelihoods shown in Fig. 8 is introduced by the numerical conversion between the distance and redshift priors performed by BILBY. While we are interested in constraining the population-level redshift

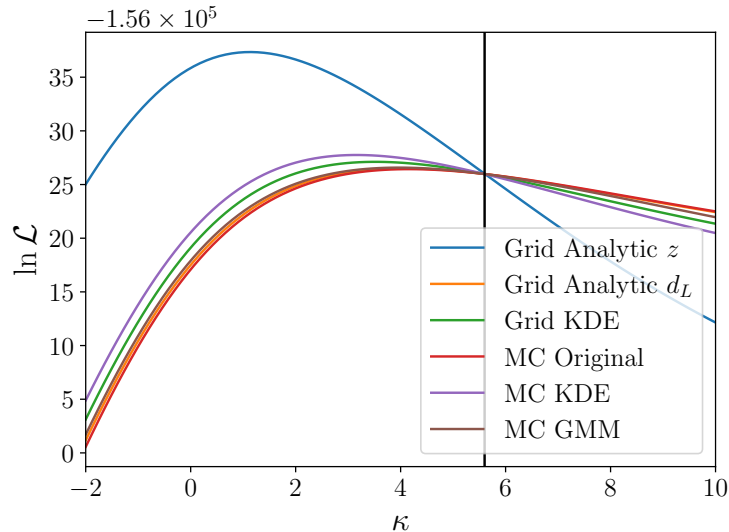


Figure 8. Log Likelihood as a function of κ for a population consisting of 500 signal segments with ξ, γ, z_p fixed to their true values for each of the six methods of evaluating Eq. 14 that we explored.

distribution, we draw injections and perform individual-event parameter estimation sampling from the corresponding luminosity distance distribution. To generate the equivalent luminosity distance prior from the Madau-Dickinson redshift distribution in Eq. 3, BILBY calculates the Jacobian $\frac{dd_L}{dz}$ numerically by taking the gradient between the luminosity distance and redshift arrays calculated using the ASTROPY cosmology module (Price-Whelan et al. 2022). We find that this conversion introduces sufficient error so that analytically reconstructing the redshift posterior from the distance likelihood as

$$p(z|d) \propto \mathcal{L}(d|d_L) \frac{dd_L}{dz} \pi(z) \quad (\text{A2})$$

leads to significant biases in the hierarchical inference likelihood (blue line in Fig. 8), while converting directly from the distance posterior to the redshift posterior (orange line in Fig. 8),

$$p(z|d) = p(d_L) \frac{dd_L}{dz}, \quad (\text{A3})$$

provides the closest match to the hierarchical likelihood calculated using MC integration over the original posterior samples.